Chinese Chemical Letters 37 (2026) 111456

Contents lists available at ScienceDirect

Chinese Chemical Letters

journal homepage: www.elsevier.com/locate/cclet

Synergistic pre-intercalation and coating engineering to realize stable Zn^{2+}/H^{+} storage in vanadium oxide cathodes for zinc-ion batteries

Yumei Wu[a,b,1], Wenbin Li[a,b,1,*], Qi Dong[a,b,1], Jianhua Zhang[a,b], Xing Huang[a,b], Haofei Yang[a,b], Siwen Zhang[a,b], Jingjing Wang[a,b], Xifei Li[a,b,c,*]

[a] Key Laboratory of Advanced Batteries Materials for Electric Vehicles of China Petroleum and Chemical Industry Federation, Institute of Advanced Electrochemical Energy & School of Materials Science and Engineering, Xi'an University of Technology, Xi'an 710048, China
[b] Shaanxi Engineering Research Center of Key Materials for Lithium/Sodium-ion Batteries, Shaanxi International Joint Research Center of Surface Technology for Energy Storage Materials, Key Laboratory of Advanced Batteries Materials for Energy Storage Materials, Key Laboratory of Advanced Batteries Materials for Electric Vehicles of China Petorleum and Chemical Industry Federation, Xi'an 710048, China
[c] Guangdong Yuanneng Technologies Co., Ltd., Foshan 528223, China

ARTICLE INFO

Article history:
Received 18 April 2025
Revised 10 June 2025
Accepted 13 June 2025
Available online 13 June 2025

Keywords:
$V_5O_{12}·6H_2O$
Layered cathode
Zinc-ion battery
Pre-intercalation
Coating

ABSTRACT

Layered $V_5O_{12}·6H_2O$ is a cathode material with great development potential for aqueous zinc-ion batteries due to its large interlayer spacing (~1.18 nm), high proportion of V^{4+}, and abundant interlayer H_2O. However, its low electronic conductivity and poor lattice stability lead to significant capacity degradation. In this regard, we develop a synergistic pre-intercalation & coating engineering, where Ni^{2+}, Mn^{2+}, or Zn^{2+} cations are pre-intercalated by one-step hydrothermal approach, and graphite oxides (GO) are coated by an electrostatic self-assembly strategy. It is found that Zn^{2+} pre-intercalation shows a better enhancement effect on the Zn^{2+}/H^{+} storage reversibility and stability, and the charge and mass transfer kinetics. Meanwhile, the synergistic effect of Zn^{2+} pre-intercalation and GO coating achieves the enhancement of the cycling performance and rate capacity with the minimal loss of initial capacities, where the discharge capacity of 288.3 and 183.3 mAh/g with the retention of 85.0 % and 61.6 % are achieved at 1 and 3 A/g after 150 and 600 cycles, respectively. The excellent electrochemical performance is attributed to the biggest downward shift of the p-band center of oxygen, the moderate radius of Zn^{2+}, and the coating of ultrathin GO with high electrical conductivity.

© 2026 Published by Elsevier B.V. on behalf of Chinese Chemical Society and Institute of Materia Medica, Chinese Academy of Medical Sciences.

With the rapid progress of solar photovoltaic technology, the nationwide installation rate of household distributed photovoltaics (PV) has witnessed a substantial increase. However, the inherent intermittency of PV power generation poses significant challenges to maintaining stable energy supply-demand balance, creating an urgent need for the development of supporting energy storage systems [1]. Aqueous zinc-ion batteries (AZIBs) have emerged as promising candidates for distributed energy storage systems, attributed to the low-cost and high-safety characteristics of their aqueous electrolytes, combined with the distinct advantages of zinc anodes: high theoretical specific capacity (820 mAh/g), low redox potential (−0.76 V *vs.* standard hydrogen electrode, SHE), and economic viability [2,3]. Research on AZIB cathodes has intensively explored diverse materials, including manganese-based compounds [4], Prussian blue analogs (PBAs) [5], vanadium-based oxides [6], and organic electroactive materials [7].

Among these, layered vanadium-based oxides have emerged as highly promising cathode materials due to their unique 2D ion storage/diffusion channels, highly tunable layered structures, multi-electron redox-active centers ($V^{3+}/V^{4+}/V^{5+}$), exceptional mechanical flexibility, and facile synthesis characteristics. Recently, layered $V_5O_{12}·6H_2O$ has attracted the attention of researchers owing to its unique stacking of bilayers (VO_6 octahedra and VO_5 square pyramids), large interlayer spacing (~1.18 nm), high proportion of tetravalent vanadium (V^{4+}), and abundant interlayer structural water, which contribute to fast Zn^{2+} storage [8]. However, challenges such as low intrinsic electronic conductivity and poor lattice stability, lead to significant capacity degradation in practical applications, making it difficult to simultaneously achieve high energy density and long cycle life.

In recent years, researchers have proposed various strategies to address the above-mentioned challenges [9]. Elemental doping

* Corresponding authors.
E-mail addresses: liwb@xaut.edu.cn (W. Li), xfli2011@hotmail.com (X. Li).
[1] These authors contributed equally to this work.

https://doi.org/10.1016/j.cclet.2025.111456
1001-8417/© 2026 Published by Elsevier B.V. on behalf of Chinese Chemical Society and Institute of Materia Medica, Chinese Academy of Medical Sciences.

modifies the electronic structure of vanadium oxides by introducing high-valent metal ions (*e.g.*, Cd [10], Mn [11], F [12]), effectively enhancing charge transport kinetics. A representative example is Cao *et al.*'s work [13], where high-valent Fe doping expands the interlayer spacing to 10.8 Å, creating fast diffusion pathways for Zn^{2+}. Interlayer engineering strategies achieve concurrent modulation of lattice and electronic structures by pre-inserting guest species. These approaches introduce structural water [14], monovalent/divalent metal ions (*e.g.*, K^+, Li^+, Na^+, Mn^{2+}, Ca^{2+}, Cu^{2+}) [15], or conductive spacers (polyaniline [16], carbon nanotubes [17]) without compromising the original crystal phase. Zhang *et al.* [18] demonstrated a sodium-ion/polyaniline co-intercalation strategy to synthesize ammonium vanadate cathodes with expanded interlayer spacing, enabling flexible ZIBs with high ionic conductivity and stable ion storage capabilities. Composite structure design (*e.g.*, V_2O_5/MXene [19], V_2O_5@GO [20]) leverages interfacial coupling effects to redistribute charge density, thereby optimizing the electronic conductivity, and suppressing the pulverization of electrode material. Notably, mono-modification strategies typically fall short of satisfying the synergistic demands for electronic conductivity and lattice stability.

Herein, we propose a synergistic pre-intercalation & coating engineering to synchronously elevate electronic conductivity and lattice stability. Concretely, we study the effects of unary Ni^{2+}, Mn^{2+}, or Zn^{2+} cations pre-intercalation on the electrochemical performance, and find that Zn^{2+} pre-intercalation shows a better enhancement effect on the Zn^{2+}/H^+ storage reversibility and stability, and the charge and mass transfer kinetics in comparison with Ni^{2+} or Mn^{2+} pre-intercalation. Meanwhile, it is found that ultrathin graphite oxide (GO) coating further amplifies these effects, and the synergistic effect of Zn^{2+} pre-intercalation and GO coating achieves the enhancement of the cycling performance and rate capacity with the minimal loss of initial specific capacities.

Ni^{2+}, Mn^{2+}, or Zn^{2+} cations, together with structural water (H_2O), were efficiently intercalated into V_5O_{12} lattice *via* a one-step hydrothermal approach, yielding NVOH, MVOH, and ZVOH sample, respectively. After that, GO coated NVOH (NVOH-GO), MVOH (MVOH-GO), and ZVOH (ZVOH-GO) samples were prepared by an electrostatic self-assembly strategy, where GO was basically not reduced, and only thinning occurred (Fig. S1 in Supporting information). The scanning electron microscopy (SEM) images in Fig. 1a and Figs. S2a and b (Supporting information) reveal that NVOH, MVOH, and ZVOH samples exhibit comparable morphological characteristics, all demonstrating a three-dimensional porous framework constructed by interconnected nanosheets. After GO treatment, it is observed that ultrathin GO was successfully coated on the surface of these nanosheets (Fig. 1b, Figs. S2c and d in Supporting information). Notably, the cation pre-intercalation and GO coating have almost no effect on the original morphologies of the three-dimensional porous framework. Transmission electron microscopy (TEM) images of ZVOH and ZVOH-GO samples (Fig. S3 in Supporting information) show that ultrathin GO uniformly encapsulates the ZVOH three-dimensional framework.

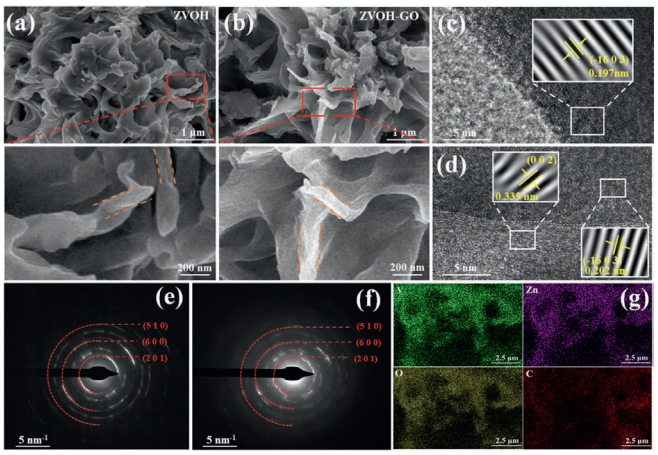


Fig. 1. SEM images of (a) ZVOH and (b) ZVOH-GO samples. HRTEM images and corresponding inverse fast Fourier transform diagrams of (c) ZVOH and (d) ZVOH-GO samples. SAED images of (e) ZVOH and (f) ZVOH-GO samples. (g) EDS images of ZVOH-GO sample.

From high-resolution TEM (HRTEM) images, the regular (−16 0 3) lattice fringes of $V_5O_{12}{\cdot}6H_2O$ lattice are observed with the interplanar spacing of 0.197 and 0.202 nm in ZVOH (Fig. 1c) and ZVOH-GO (Fig. 1d) samples, respectively. Notably, the (002) lattice fringes of GO are simultaneously observed with the interplanar spacing of 0.335 nm on the surface of ZVOH nanosheets in ZVOH-GO sample (Fig. 1d), directly demonstrating the successful coating of GO. Notably, the (−16 0 3) lattice fringes in ZVOH-GO sample are slightly more blurred compared to those in ZVOH sample, which is in good agreement with GO coating. The corresponding selected area electron diffraction (SAED) patterns in Figs. 1e and f display concentric diffraction rings of (510), (600) and (201) crystal planes, corroborating their polycrystalline characteristics. Energy-dispersive spectroscopy (EDS) mapping of ZVOH-GO sample (Fig. 1g) reveals uniform elemental distributions of V, O, Zn, and C on the three-dimensional porous framework, and the distribution of element C shows a relatively dispersed phenomenon, corroborating the successful Zn^{2+} pre-intercalation and GO coating.

X-ray diffraction (XRD) analysis (Fig. 2a and Fig. S4 in Supporting information) validates that the six samples strongly suggest the monoclinic $V_5O_{12}{\cdot}6H_2O$ phase (JCPDS No. 45–1401), where the three strongest diffraction peaks of (001), (210) and (021) crystal planes are clearly observed at ~7.5°, 25.2° and 51.4°, respectively. This indicates that the cation pre-intercalation and GO coating have almost no effect on the original lattice framework. Notably, the (001) diffraction peaks of all synthesized samples shift to lower angles relative to pure $V_5O_{12}{\cdot}6H_2O$ phase, indirectly indicating the successfully pre-intercalation of Ni^{2+}, Mn^{2+}, or Zn^{2+} with the interlayer spacing expansion. Meanwhile, the large Mn^{2+} radius (0.83 Å) enables MVOH and MVOH-GO samples to exhibit a larger interlayer spacing than NVOH/MVOH-GO (Ni^{2+}: 0.69 Å), and ZVOH/ZVOH-GO (Zn^{2+}: 0.74 Å) samples.

Inductively coupled plasma atomic emission spectroscopy (ICP-AES) data in Table S1 (Supporting information) reveal that the atomic ratios of Ni:V_5O_{12}, Mn:V_5O_{12} and Zn:V_5O_{12} are 0.40:1, 0.35:1, and 0.38:1 for NVOH, MVOH and ZVOH samples, respectively. This demonstrates a similar amount of pre-intercalated Ni^{2+}, Mn^{2+}, or Zn^{2+} cations with low-concentration. Meanwhile, these ratios are 0.44:1, 0.41:1 and 0.38:1 for NVOH-GO, MVOG-GO and ZVOH-GO samples, respectively, declaring that GO coating process have a very small effect on the pre-intercalated cations. Thermogravimetric analysis (TGA) calculations (Fig. 2b) indicate that NVOH, MVOH, and ZVOH samples contain lattice water at mass percentages of 6.95 wt%, 6.57 wt% and 9.28 wt%, respectively. These results enable the derivation of stoichiometric formulas: $Ni_{0.44}V_5O_{12}{\cdot}1.96H_2O$ (NVOH), $Mn_{0.41}V_5O_{12}{\cdot}1.83H_2O$ (MVOH) and $Zn_{0.38}V_5O_{12}{\cdot}2.56H_2O$ (ZVOH). Meanwhile, NVOH, MVOH and ZVOH mass fractions are calculated to be 91.2 wt%, 91.1 wt%, and 87.51 wt% in NVOH-GO, MVOH-GO and ZVOH-GO samples, respectively (Fig. 2c).

X-ray photoelectron spectroscopy (XPS) was utilized to characterize the elemental composition and chemical states of the six samples. Survey scans of NVOH, MVOH and ZVOH samples confirm the presence of Ni/V/O, Mn/V/O, and Zn/V/O elemental combinations, respectively (Fig. S5a in Supporting information). Following GO coating, NVOH-GO, MVOH-GO and ZVOH-GO samples retain their original Ni/V/O, Mn/V/O and Zn/V/O compositions

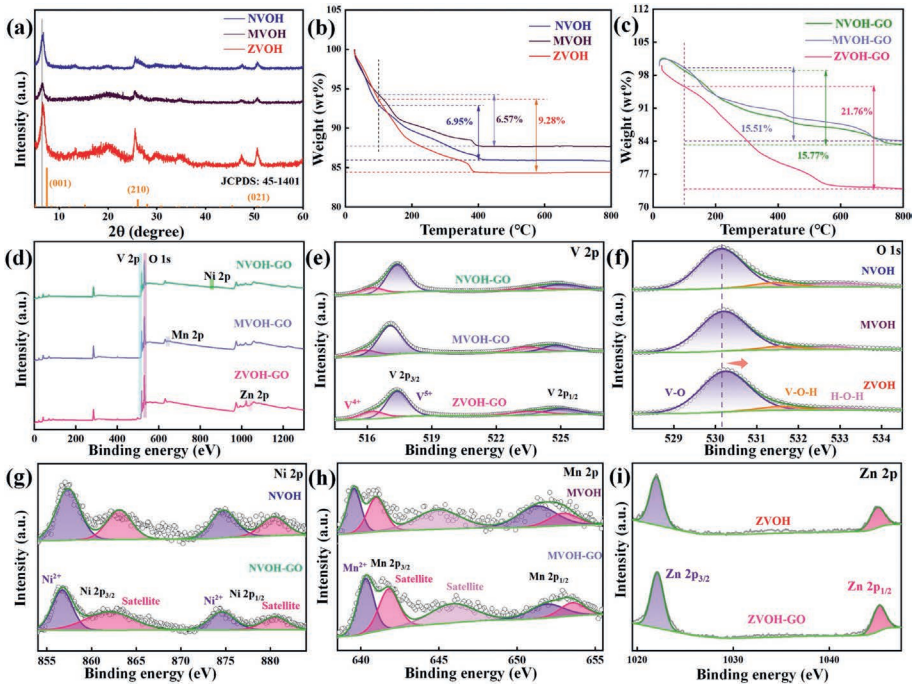


Fig. 2. (a) XRD patterns, (b) TGA curves and (f) high-resolution O 1s XPS spectra of NVOH, MVOH and ZVOH samples. (c) TGA curves, (d) survey and (e) high-resolution V 2p XPS spectra of NVOH-GO, MVOH-GO and ZVOH-GO samples. (g) High-resolution Ni 2p XPS spectra of NVOH and NVOH-GO samples. (h) High-resolution Mn 2p XPS spectra of MVOH and MVOH-GO samples. (i) High-resolution Zn 2p XPS spectra of ZVOH and ZVOH-GO samples.

(Fig. 2d). This again demonstrates the successful pre-intercalation of Ni^{2+}, Mn^{2+}, or Zn^{2+} cations. Fig. 2e and Fig. S5b (Supporting information) present the dual contributions originating from V^{5+} (~517.1/524.4 eV, V $2p_{1/2}$) and V^{4+} (~515.3/522.6 eV, V $2p_{3/2}$) [21]. The emergence of V^{4+} serves to balance the charge alteration following the pre-intercalation of cations and absence of oxygen. Notably, the pre-intercalation of Zn^{2+} cations leads to a significant increase in the V^{4+} proportion (25 % in ZVOH-GO sample *vs.* 21 % for Ni^{2+} in NVOH-GO sample and 19 % for Mn^{2+} in MVOH-GO sample, Table S2 in Supporting information), indicating a substantial enhancement in the electrical conductivity of ZVOH-GO sample. Meanwhile, GO coating increases the V^{4+} proportions, which may be related to the charge transfer from GO's π-conjugated system to the V-O framework, corroborated by C 1s → V 3d orbital interactions. In Fig. 2f, three distinct peaks are detected at ~530, 532, and 533 eV, assigned to V-O bonds within the V_5O_{12} layers, V-O-H bonds from interlayer water molecules, and H–O-H bonds from adsorbed water molecules, respectively [22]. ZVOH sample shows a positive shift of V-O peak compared with NVOH and MVOH samples, indicating a downward shift of the p-band center (ε_p) of O.

In the high-resolution Ni 2p XPS spectra of NVOH and NVOH-GO samples, only Ni^{2+} signals are probed at ~857 and 874 eV corresponding to Ni $2p_{3/2}$ and $2p_{1/2}$ peaks, respectively (Fig. 2g) [23]. In the high-resolution Mn 2p XPS spectra of MVOH and MVOH-GO samples, only Mn^{2+} signals are probed at ~641.2 and 653.8 eV corresponding to Mn $2p_{3/2}$ and $2p_{1/2}$ peaks, respectively (Fig. 2h) [24]. Notably, the appearance of some satellite peaks is attributed to the orbital hybridization between pre-intercalated Ni^{2+}/Mn^{2+} and lattice oxygen within the V_5O_{12} layers, reflecting the electronic interactions induced by ligand-metal charge transfer mechanisms. In the high-resolution Zn 2p XPS spectra of ZVOH and ZVOH-GO samples, only Zn^{2+} signals are probed at ~1022 and 1045.3 eV corresponding to Zn $2p_{3/2}$ and $2p_{1/2}$ peaks, respectively (Fig. 2i) [25]. As a result, the cation pre-intercalation process does not change the pristine valence states of Ni^{2+}/Mn^{2+}/Zn^{2+} in the starting materials, and GO coating process have almost no effect on the pre-intercalated cations.

Ex-situ XRD patterns of ZVOH-GO cathode in Fig. 3a and corresponding waterfall plots in Fig. 3b reveal that the (001) diffraction signal from $V_5O_{12}{\cdot}6H_2O$ at ~6.4° becomes very weak during the initial discharging process and does not recover during the reverse charging process. As a comparison, the (210) diffraction peak from $V_5O_{12}{\cdot}6H_2O$ at ~25.3° is basically maintained throughout the discharging-charging process. The two points jointly claim that ZVOH-GO cathode material is peeled off, but no phase transformation has occurred during the discharging-charging process. This corresponds well to the electrochemical mechanism of the intercalation reaction. Meanwhile, the diffraction signal from $Zn_x(CF_3SO_3)_y(OH)_{2x-y}{\cdot}nH_2O$ (ZCH) precipitate at $2\theta = 12.29°$ appears after discharging to 1.5 V. Additionally, the *ex-situ* SEM image in Fig. 3c recorded at discharge state of 1.2 V reveals abundant aggregated lamellar ZCH precipitates on the cathode surface, confirming the H^+ intercalation reaction at high potentials that induces the generation of OH^- with the formation of ZCH precipitate. After further discharging to 1.0 V, the ZCH signal disappears, which may be attributed to Zn^{2+} intercalation reaction at low potentials. The deep Zn^{2+} intercalation reduces the local Zn^{2+} concentration in the electrolyte, which drives ZCH dissociation and allows it to re-enter the electrolyte. As the discharge voltage drops to 0.3 V, a small amount of ZCH precipitate reappears with a dispersed micro-flake morphology, which may be highly correlated with the dynamic supplementation of Zn^{2+} from the electrolyte. During the reverse-charging process from 0.3 V to 1.7 V, ZCH precipitate undergoes the opposite processes of redissolution and redeposition. After charging to 1.5 V, the lamellar ZCH precipitates reaggregate and deposit. *In-situ* electrochemical impedance spectra (EIS) in Fig. 3d show that the charge transfer resistance (R_{ct}) firstly increases, then decreases and finally increases during the discharging process from 1.7 V to 0.3 V. Meanwhile, the opposite variation laws occur during the reverse charging process. Thus, the morpho-

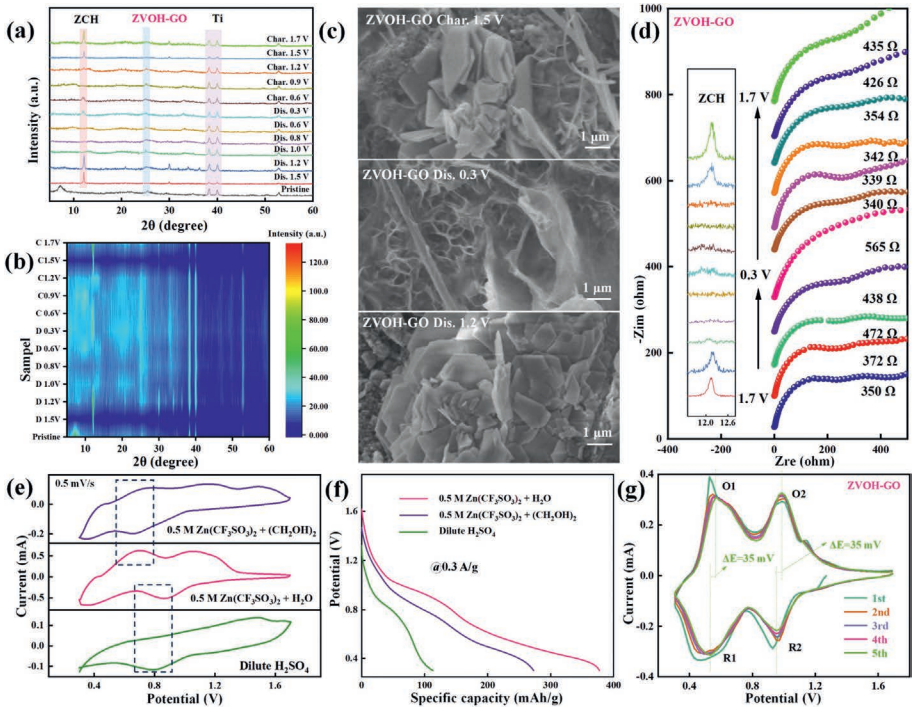


Fig. 3. (a) *Ex-situ* XRD patterns and corresponding (b) waterfall diagram. (c) *Ex-situ* SEM images. (d) *In-situ* EIS spectra and locally magnified *ex-situ* XRD patterns. (e) CV curves and (f) discharge profiles tested by button cell with different electrolytes. (g) The initial five CV curves at 0.1 mV/s for ZVOH-GO cathode.

logical evolution of ZCH precipitates and the R_{ct} change of the battery correspond well to the *ex-situ* XRD result of the cathode.

To further elucidate the electrochemical mechanism of ZVOH-GO cathode, the cyclic voltammetry (CV) curves and discharge profiles were systematically compared in three electrolytes: 0.5 mol/L $Zn(CF_3SO_3)_2 + H_2O$ (H^+/Zn^{2+}-containing), 0.5 mol/L $Zn(CF_3SO_3)_2 + (CH_2OH)_2$ (Zn^{2+}-only) and dilute H_2SO_4 (H^+-only, pH 4.55). Notably, CV curves in Fig. 3e directly corroborate H^+ intercalation at high potentials and Zn^{2+} intercalation at low potentials through peak position analysis across the three electrolytes. Discharge profiles in Fig. 3f reveal that the specific capacity in the electrolyte of 0.5 mol/L $Zn(CF_3SO_3)_2 + H_2O$ (377.7 mAh/g) is approximately equal to the sum of the specific capacities in 0.5 mol/L $Zn(CF_3SO_3)_2 + (CH_2OH)_2$ and dilute H_2SO_4, corresponding well to the energy storage process of H^+/Zn^{2+} co-intercalation. Thus, ZVOH-GO cathode exhibits the electrochemical mechanism of H^+ intercalation and followed Zn^{2+} intercalation, and the dissolution and deposition of ZCH occur simultaneously. As presented in Fig. S6a (Supporting information), Zn^{2+} storage contributions at 0.1 A/g are 56%–60% for the six cathodes. Meanwhile, the H^+ storage contributions increase slightly with the increase of the rate from 0.1 A/g to 1 A/g, and increase markedly at 3 A/g (Fig. S6b in Supporting information), which well corresponds to its faster electrochemical kinetics than Zn^{2+} storage.

CV curves at 0.1 mV/s (Fig. 3g, Figs. S7 and S8 in Supporting information) show the six cathodes display two well-defined pairs of redox peaks at ~0.94/1.02 and 0.50/0.61 V, corresponding to sequential H^+ and Zn^{2+} intercalation reactions, respectively. This declares that the cation pre-intercalation and GO coating do not alter the fundamental electrochemical mechanism. Notably, with prolonged CV cycling, a systematic attenuation of R2 peaks is observed, corroborating the gradual deterioration of H^+ intercalation reaction. As a comparison, Zn^{2+} intercalation reaction is relatively stable (R1 peaks), and ZVOH-GO cathode displays the most stable Zn^{2+} intercalation reaction among the six cathodes. This declares that Zn^{2+} pre-intercalation enhances the Zn^{2+} storage stability, and GO coating further amplifies this effect. Besides, ZVOH-GO cathode presents the smallest potential differences (ΔE) between oxidation (O1, O2) and reduction (R1, R2) peaks in the 5th-cycle CV, and GO coating decreases the corresponding ΔE_s. This suggests that Zn^{2+} pre-intercalation significantly improves the reversibility of both Zn^{2+} and H^+ intercalation reactions in comparison with Ni^{2+} or Mn^{2+} pre-intercalation, and GO coating further amplifies this effect.

As displayed in Fig. 4a, ZVOH-GO cathode delivers a discharge capacity of 412.7 mAh/g at 0.1 A/g and retains 112.5 mAh/g at 5 A/g, significantly outperforming NVOH-GO (368.6/69.4 mAh/g) and MVOH-GO (409.3/104.2 mAh/g) cathodes. Meanwhile, ZVOH cathode exhibits significantly higher rate capacities than NVOH and MVOH cathodes (Fig. S9 in Supporting information), which are lower than the corresponding ZVOH-GO, NVOH-GO and MVOH-GO cathodes. Besides, ZVOH-GO cathode also presents the highest capacity retention across various rates (Fig. 4b). The three aspects validate that Zn^{2+} pre-intercalation significantly enhances the rate capability in comparison with Ni^{2+} or Mn^{2+} pre-intercalation, and GO coating further amplifies this effect. Notably, as the rate increases from 0.1 A/g to 0.5 A/g, the two pairs of redox peaks can always be clearly displayed in these dQ/dV curves of Fig. S10 (Supporting information) for ZVOH-GO, NVOH-GO, MVOH-GO and ZVOH cathodes, indicating their well Zn^{2+} and H^+ storage stability at low rates. Meanwhile, the electrochemical polarization of H^+ intercalation at high potentials is weaker than that of Zn^{2+} intercalation at low potentials, agreeing well with the electrochemical mechanism of H^+ and followed Zn^{2+} intercalation.

As displayed in Fig. S11 (Supporting information), the pristine ZVOH, MVOH and NVOH cathodes deliver similar initial capacities at 1 A/g, whereas undergo rapid capacity decay during cycling process of 150 cycle with the sequence of NVOH > MVOH > ZVOH. As a result, Zn^{2+} pre-intercalation improves the cycling stability, followed by Mn^{2+} and Ni^{2+} pre-intercalation. After GO coating, the initial capacities of ZVOH-GO cathode slightly reduce, but those of NVOH-GO and MVOH-GO cathodes obviously reduce

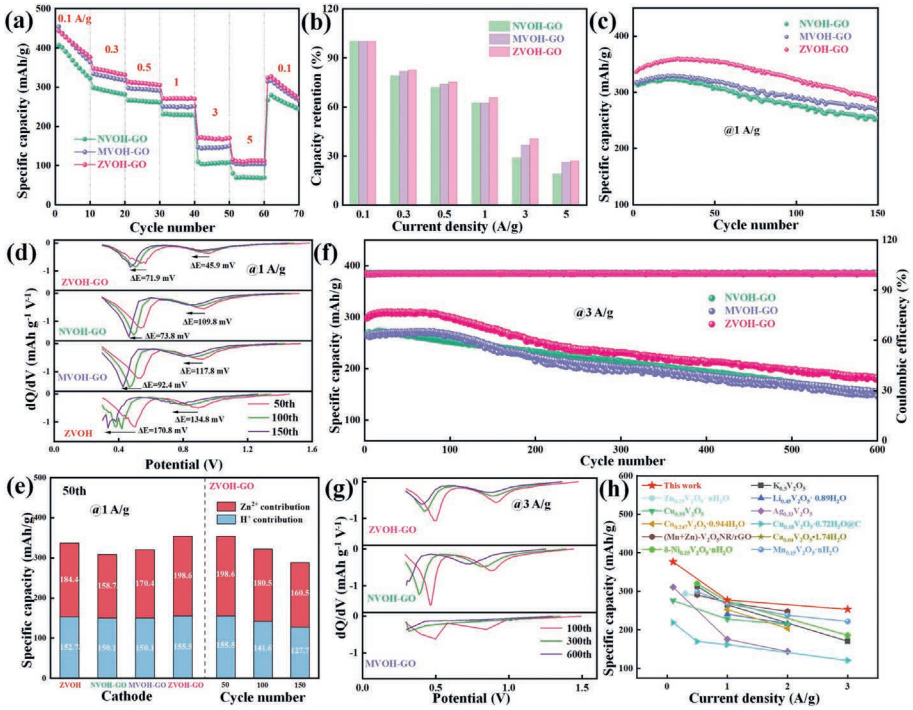


Fig. 4. (a) Rate capabilities and corresponding (b) capacity retentions across various rates, cycling performances at (c) 1 A/g and (f) 3 A/g, and (g) the 100th, 300th and 600th d*Q*/d*V* curves at 3 A/g for NVOH-GO, MVOH-GO and ZVOH-GO cathodes. (d) The 50th, 100th and 150th d*Q*/d*V* curves at 1 A/g for ZVOH-GO, NVOH-GO, MVOH-GO and ZVOH cathodes. (e) Zn^{2+} and H^+ storage capacities of ZVOH-GO, NVOH-GO, MVOH-GO and ZVOH cathodes, and Zn^{2+} and H^+ storage capacities of ZVOH-GO cathode at the 50th, 100th and 150th cycles at 1 A/g. (h) Capacity comparison of ZVOH-GO cathode with the ever-reported layered vanadium-based oxide cathodes.

(Fig. 4c). This phenomenon is attributed to the mass proportion of inactive GO. Notably, the capacity decay behaviors are substantially suppressed (ZVOH-GO: 70.2 % → 85.0 %, NVOH-GO: 59.9 % → 80.4 %, MVOH-GO: 59.6 % → 83.3 %), and ZVOH-GO cathode maintains the highest capacity retention of 85.0 % and discharge capacity of 288.3 mAh/g (NVOH-GO: 253.8, MVOH-GO: 264.9) after 150 cycles. Thus, GO coating significantly improves the cycling stability, whose effect is better than that of cation pre-intercalation. Especially, the synergistic effect of Zn^{2+} pre-intercalation and GO coating achieves the enhancement of stability with the minimal loss of initial specific capacities. d*Q*/d*V* curves in Fig. 4d reveal that ZVOH-GO cathode exhibits the smallest electrochemical polarization for Zn^{2+} (71.9 mV) and H^+ (45.9 mV) storage, which is proved by the potential differences of the discharge peaks between the 50th and 150th cycles (NVOH-GO: 73.8/109.8, MVOH-GO: 92.4/117.8, ZVOH: 170.8/134.8). Meanwhile, ZVOH-GO cathode exhibits the synchronously increasing Zn^{2+} and H^+ storage capacities compared with NVOH-GO, MVOH-GO and ZVOH cathodes, and the synchronously decaying Zn^{2+} and H^+ storage capacities with the number of cycles rising from 50 to 150 (Fig. 4e). These two aspects declare that Zn^{2+} pre-intercalation and GO coating concurrently improve Zn^{2+} and H^+ storage stability during the cycling processes of 150 cycles at 1 A/g.

The long-cycling performances at a high current density of 3 A/g in Fig. 4f show that ZVOH-GO cathode still delivers the highest initial capacities, and the largest capacity retention of 61.6 % and discharge capacity of 183.3 mAh/g after 600 cycles (NVOH-GO: 57.6/153.3, MVOH-GO: 55.5/146.7). This capacity decay is attributed to the irreversible accumulation of ZCH precipitate (Fig. S12 in Supporting information) that leads to the increase in polarization degree (Fig. 4g), and the irreversible exfoliation of the (001) crystal plane (Fig. 3a). Notably, *dQ*/*dV* curves in Fig. 4g reveal that ZVOH-GO cathode also exhibits the smallest electrochemical polarization for Zn^{2+} and H^+ storage compared with NVOH-GO and MVOH-GO cathodes. Meanwhile, ZVOH-GO cathode exhibits the synchronously increasing Zn^{2+} and H^+ storage capacities, and the synchronously decaying Zn^{2+} and H^+ storage capacities with the number of cycles rising from 100 to 600 (Fig. S13 in Supporting information). When compared to previously reported layered vanadium-based oxide cathodes, ZVOH-GO cathode exhibits competitive cycling performance, particularly at the high current densities of 3 A/g (Fig. 4h and Table S3 in Supporting information).

As presented in Fig. S14 (Supporting information) and Fig. 5a, ZVOH cathode demonstrates the lowest R_{ct} of 600 Ω, trailed by NVOH cathode at 911.2 Ω and MVOH cathode at 942.8 Ω. After GO coating, the corresponding R_{ct}s decrease, and ZVOH-GO cathode still demonstrates the smallest R_{ct} of 414 Ω, succeeded by NVOH-GO at 605.6 Ω and MVOH-GO at 656 Ω. Meanwhile, the fitting results of the relationship between Z_{re} and $\omega^{-1/2}$ ($\omega = 2\pi f$) in Fig. 5b illustrate that ZVOH cathode features a lower diffusion resistance ($Z_W = 27.2\ \Omega\ s^{1/2}$) than NVOH (40.4 Ω $s^{1/2}$) and MVOH (55.7 Ω $s^{1/2}$) cathodes, and ZVOH-GO cathode displays the smallest Z_W (22.0 Ω $s^{1/2}$). These two aspects declare that Zn^{2+} pre-intercalation accelerates the charge and mass transfer kinetics, and GO coating further amplifies this effect. Discharge galvanostatic intermittent titration technique (GITT) profiles in Fig. S15 (Supporting information), combined with the ion diffusion coefficients (D_s) calculated using Eq. S1 (Supporting information) in Fig. 5c reveal two distinct diffusion behaviors: Rapid ion transport at high voltages and sluggish diffusion at low voltages, corresponding to fast H^+ storage and slow Zn^{2+} storage kinetics, respectively. Notably, Zn^{2+} pre-intercalation yields higher D_s compared to Mn^{2+} or Ni^{2+} pre-intercalation.

As shown in Fig. 5d and Fig. S16 (Supporting information), the two reduction peaks gradually broaden with increasing scan rates from 0.2 mV/s to 1.0 mV/s, with the peaks shifted to lower potentials, and the characteristic shapes of Peak R1 show more obvious distortion than those of Peak R2, corresponding to better kinetics of H^+ than Zn^{2+} intercalation. Notably, ZVOH cathode shows a

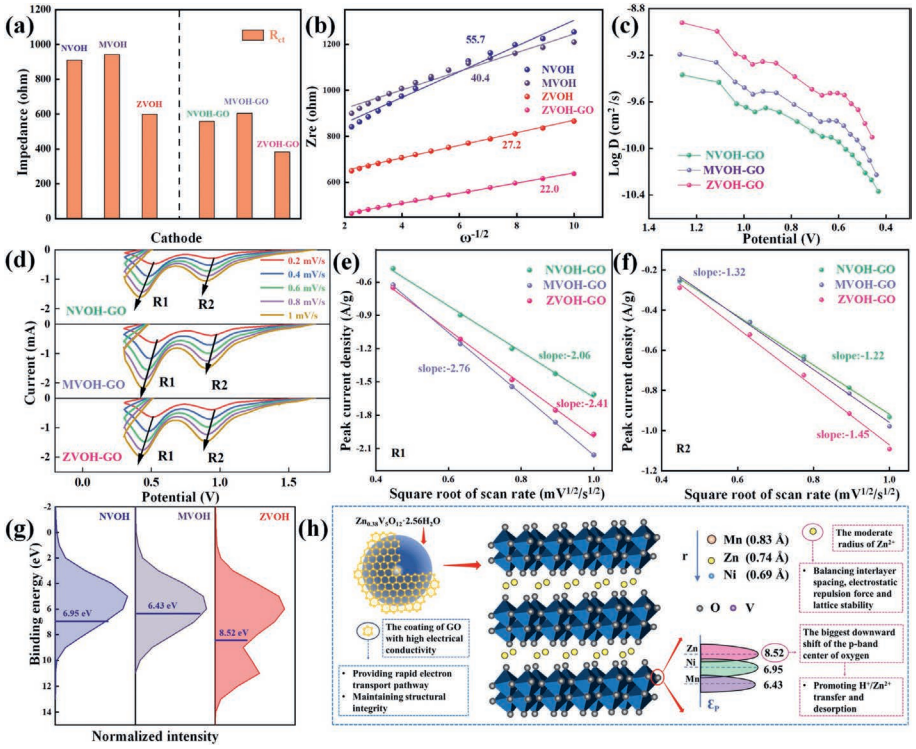


Fig. 5. (a) Fitted R_{ct}s of the six cathodes. (b) Fitting curves between Z_{re} and $\omega^{-1/2}$ for NVOH, MVOH, ZVOH and ZVOH-GO cathodes. (c) D_s, (d) multi-scan rate CV reduction curves, and relationships between peak current and square root of scan rate for (e) Peak R1 and (f) Peak R2 for NVOH-GO, MVOH-GO and ZVOH-GO cathodes. (g) VBS (the blue bars show the ε_p of O) for ZVOH, NVOH and MVOH cathodes. (h) Schematic diagram of the synergistic enhancement mechanism of cation pre-intercalation and GO coating on electrochemical performance.

weaker distortion of Peak R1 and a smaller shift of Peak R2 compared to those of NVOH and MVOH cathodes, and ZVOH, NVOH and MVOH cathodes show a greater distortion of Peak R1 and a more pronounced shift of Peak R2 compared to that of ZVOH-GO, NVOH-GO and MVOH-GO cathodes. This suggests that Zn^{2+} pre-intercalation and GO coating weaken the electrochemical polarization, and the effects of GO coating are better than that of cation pre-intercalation, corroborating the superior rate capability of ZVOH-GO cathode. Post-processing of CV curves using Eq. S2 (Supporting information) reveal a linear correlation between peak current (i_p) and square root of scan rate ($v^{1/2}$) (Figs. 5e and f, Fig. S17 in Supporting information). Fitted slope values of Peak R1/R2 are −1.63/−1.17, −2.26/−1.29, −1.69/−1.39, −2.06/−1.22, −2.76/−1.32, and −2.41/−1.45 for NVOH, MVOH, ZVOH, NVOH-GO, MVOH-GO and ZVOH-GO cathodes, respectively. As a result, GO coating simultaneously enhances the Zn^{2+}/H^+ storage kinetics considering the improvement of electron conduction, and Zn^{2+} and Mn^{2+} pre-intercalation enhances H^+ and Zn^{2+} storage kinetics considering the combined effect of electron and ion conduction, respectively.

Taking all the above analysis into account, the synergistic enhancement mechanism of cation pre-intercalation and GO coating is summarized as follows. On the one hand, to better understand the enhancement mechanism of cation pre-intercalation on electrochemical performance, valence band spectrum (VBS) analysis was carried out. As presented in Fig. 5g, Zn^{2+} pre-intercalated ZVOH exhibits the biggest downward shift of oxygen ε_p with a value of 8.52 eV compared to Ni^{2+} (NVOH: 6.95 eV) and Mn^{2+} (MVOH: 6.43 eV) pre-intercalated systems. As a result, ZVOH cathode demonstrates the weakest binding between lattice O and Zn^{2+}/H^+, which endows it with dual advantages of the strongest H^+/Zn^{2+} transfer and desorption ability. Meanwhile, the moderate radius (0.74 Å) of Zn^{2+} balances the expansion of the interlayer spacing that can promote Zn^{2+}/H^+ diffusion, the electrostatic repulsion force that can hinder Zn^{2+}/H^+ diffusion, and the lattice stability compared to Ni^{2+} (0.69 Å) and Mn^{2+} (0.83 Å) that may cause serious local lattice distortion. Especially, in the AZIBs, Zn^{2+} is the main energy storage ions, the pre-intercalation of the Zn^{2+} with moderate radius can create an appropriately sized interlayer space suitable for Zn^{2+} storage and transport. As a comparison, the interlayer space created by Mn^{2+} with larger radius is suitable, but the electrostatic repulsion is too strong. Meanwhile, although the electrostatic repulsion is weak, the interlayer space created by Ni^{2+} with smaller radius is too small for Zn^{2+} storage. On the other hand, the sp^2 carbon domains of GO provide a rapid electron transport pathway, compensating for the intrinsic low electrical conductivity of cation pre-intercalated $V_5O_{12}{\cdot}6H_2O$. Meanwhile, GO coating suppresses the volume changes and further pulverization of electrode material during cycling, maintaining structural integrity (Fig. 5h).

In summary, we successfully synthesize unary Ni^{2+}, Mn^{2+}, or Zn^{2+} cations pre-intercalated $V_5O_{12}{\cdot}6H_2O$ by one-step hydrothermal approach, and further achieve the GO coating by an electrostatic self-assembly strategy. Cation pre-intercalation and GO coating have almost no effect on the original morphologies and lattice framework. Zn^{2+}pre-intercalation shows a better enhancement effect on the Zn^{2+}/H^+ storage reversibility and stability, and the charge and mass transfer kinetics, and GO coating further amplifies these effects. The synergistic effect of Zn^{2+} pre-intercalation and GO coating achieves the enhancement of the cycling performance and rate capacity with the minimal loss of initial specific capacities. ZVOH-GO cathode presents the largest discharge capacity of 288.3 and 183.3 mAh/g with the highest capacity retention of 85.0 and 61.6% after 150 and 600 cycles at 1 and 3 A/g, respectively. The excellent electrochemical performance is attributed to the biggest downward shift of the p-band center of oxygen, the moderate radius of Zn^{2+}, and the coating of ultra-

thin GO with high electrical conductivity. Comprehensively, the enhancement effects of GO coating on cycling stability are better than those of cation pre-intercalation. ZVOH-GO cathode exhibits the electrochemical mechanism of H^+ intercalation and followed Zn^{2+} intercalation with the dissolution and deposition of ZCH.

CRediT authorship contribution statement

Yumei Wu: Writing – original draft, Validation, Software, Methodology, Investigation, Formal analysis, Data curation. **Wenbin Li:** Writing – review & editing, Supervision, Methodology, Formal analysis, Conceptualization. **Qi Dong:** Visualization, Supervision, Methodology, Investigation, Formal analysis, Data curation. **Jianhua Zhang:** Software, Resources. **Xing Huang:** Resources, Data curation. **Haofei Yang:** Software, Investigation. **Siwen Zhang:** Writing – original draft. **Jingjing Wang:** Project administration, Funding acquisition. **Xifei Li:** Project administration, Conceptualization.

Declaration of competing interest

The authors declare that they have no known competing financial interests or personal relationships that could have appeared to influence the work reported in this paper.

Acknowledgments

This work was supported by National Natural Science Foundation of China (Nos. 52103348, 52272237, 52104313), Qin Chuangyuan "Scientist+Engineer" team construction program of Shaanxi Province (No. 2024QCY-KXJ-146), Key Research and development program of Xianyang City (No. L2024-ZDYF-ZDYF-GY-0028), China Postdoctoral Science Foundation (No. 2021M692596), Key Research and Development Program of Shaanxi Province (No. 023-YBGY-449), Scientific Research Program Funded by Shaanxi Provincial Education Department (No. 23JC055), National Innovation and Entrepreneurship Training Program for Undergraduates (No. 202410700052X), Research Startup Funding for Shaanxi Provincial Outstanding Young Talents Support Program (Universities), Science and technology guidance program of China Petroleum and Chemical Industry Federation, Foshan Science and Technology Innovation Team Project (No. 1920001004098).

Supplementary materials

Supplementary material associated with this article can be found, in the online version, at doi:10.1016/j.cclet.2025.111456.

References

[1] Y. Liu, F. Wang, Z. Jiao, et al., Electrochem. Energy Rev. 5 (2022) 5.
[2] Z. Yi, G. Chen, F. Hou, L. Wang, J. Liang, Adv. Energy Mater. 11 (2021) 2003065.
[3] W. Li, Q. Song, Q. Dong, et al., Adv. Mater. 37 (2024) 2414019.
[4] N. Zhang, J.C. Wang, Y.F. Guo, et al., Coord. Chem. Rev. 479 (2023) 215009.
[5] Y. Yang, J. Zhou, L. Wang, et al., Nano Energy 99 (2022) 107424.
[6] L. Jia, H. Hu, X. Cheng, et al., Adv. Energy Mater. 14 (2024) 2304010.
[7] R. Yuksel, O. Buyukcakir, W.K. Seong, R.S. Ruoff, Adv. Energy Mater. 10 (2020) 1904215.
[8] N. Zhang, M. Jia, Y. Dong, et al., Adv. Funct. Mater. 29 (2019) 1807331.
[9] A. Guo, Z. Wang, L. Chen, et al., ACS Nano 18 (2024) 27261–27286.
[10] T. Chen, Q. Wu, L. Lang, et al., Chem. Eng. J. 499 (2024) 156295.
[11] H. Wang, R. Guo, Y. Ma, F. Zhou, Adv. Funct. Mater. 33 (2023) 2301351.
[12] S. Deng, X. Yan, Y. Jiang, et al., Chem. Eng. J. 503 (2025) 158472.
[13] F. Wu, Y. Wang, P. Ruan, et al., Mater. Today Energy 21 (2021) 100842.
[14] C. Li, X. Jiang, H. Qi, et al., Energy Storage Mater. 75 (2025) 104012.
[15] H. Geng, M. Cheng, B. Wang, et al., Adv. Funct. Mater. 30 (2020) 1907684.
[16] Z. Liu, B. Sun, Y. Zhang, Q. Zhang, L. Fan, Prog. Polym. Sci. 152 (2024) 101817.
[17] F. Wan, S. Huang, H. Cao, Z. Niu, ACS Nano 14 (2020) 6752–6760.
[18] S. Zhao, S. Wang, J. Guo, et al., Adv. Funct. Mater. 33 (2023) 2305700.
[19] Y. Mei, Y. Liu, W. Xu, et al., Chem. Eng. J. 452 (2023) 139574.
[20] J. Wang, J.G. Wang, H. Liu, et al., Adv. Funct. Mater. 31 (2021) 2007397.
[21] N. Zhang, Y. Dong, M. Jia, et al., ACS Energy Lett. 3 (2018) 1366–1372.
[22] S. Shen, D. Ma, K. Ouyang, et al., Adv. Funct. Mater. 33 (2023) 2304255.
[23] Y. Liu, J. Lv, T. Cao, Y. Gong, D. Zhang, Chem. Eng. J. 441 (2022) 136007.
[24] H. Geng, M. Cheng, B. Wang, et al., Adv. Funct. Mater. 30 (2020) 1907684.
[25] D. Kundu, B.D. Adams, V. Duffort, S.H. Vajargah, L.F. Nazar, Nat. Energy 1 (2016) 8.